A Mach-Zehnder phasing sensor for extremely large segmented telescopes: Laboratory results and close loop algorithm

Natalia Yaitskova[*a], Luzma Montoya-Martinez[b], Kjetil Dohlen[b], Philippe Dierickx[a]

[a]European Southern Observatory, Karl Schwarzschildstr. 2, 85748 Garching bei Munchen, Germany
[b]Laboratoire d'Astrophysique de Marseille, 2 Place Leverrier - 13248 Marseille Cedex 4 - FRANCE

ABSTRACT

Alignment of the segmented telescopes requires an accurate phase measurement at the segment borders using an optical sensor. We develop such a sensor based on the Mach-Zehnder interferometer. The operation of this system was previously demonstrated in computer simulation and through the detailed theoretical analysis. In this paper we show the results of the laboratory experiment, which confirms the main predictions we have made. The close loop control for optical phasing of segmented mirrors, analogous to the one with the use of the edge sensors, is also described and illustrated.

Keywords: telescopes, segmentation, phasing, wavefront control, diffraction.

1. INTRODUCTION

Projects for future extremely large telescopes (ELTs) rely on the giant segmented mirrors. The current design of 100m OWL project [1] assumes a 100m primary mirror consisting of 3048 hexagonal segments with 1.6m flat-to-flat width. The secondary mirror of OWL is 26m in diameter, consisting of 234 segments identical to those of the primary mirror.

One of the critical tasks associated with the giant telescope is phasing of their segmented surfaces. To achieve the resolution commensurable with the monolith telescope of the same diameter the segments must be phased with the precision better than 10nm surface rms [2,3]. Three principal hardware systems are requited for the segment active control [4]: positioning sensors provide real time information about segment relative displacements; segment actuators compensate for these displacements; a phasing camera provides the periodical calibration of sensors' readings. Three new alignment concepts as an alternative to the Keck phasing camera are being currently investigated, based on the principle of pupil plane sensing: the curvature sensor [5,6], the pyramid sensor [7], and a Mach-Zehnder interferometer [8,9]. In all optical methods the signal is well located near the intersegment baundary and proportional to the local phase step. So far our group was involved into the study of the Mach – Zehnder interferometer. The comparative analysis of all three techniques together with the classical Schack – Hartmann sensor is the subject of the planed Active Phasing Experiment (APE) [10].

The thorough theoretical study and the direct numerical simulation were presented in our previous publications [8,9]. In this paper we present some new results. Section 2 is devoted to the laboratory demonstration of the Mach-Zehnder interferometer. In this experiment the phase step measurement was performed also with the use of the turbulent generator to verify the possibility of the optical phasing the in the condition of the turbulence.

In the section 3 we describe a new method for piston, tip and tilt reconstruction from the interferometric signal. This algorithm uses the symmetric and anti-symmetric properties of the signal and links the optical phase measurement to the one provided by the edge sensors. Applying the standard close loop control method on the signals obtained at the output of the interferometer we simulate the phasing of the segmented mirrors.

[*] nyaitsko@eso.org, phone +49 89 3200 6581

2. LABORATORY TEST OF THE MACH-ZEHNDER CO-PHASING TECHNIQUE

2.1 Exposition

The principal scheme of the Mach-Zehnder interferometer is shown in Figure 1. The incoming from the telescope focus beam is split in two arms. A pinhole placed in the focal plane of the one arm acts as a spatial filter providing the reference wave coherent to the incoming wave. The two beams are recombined and form two complementary interference patterns recorded by two imaging detectors. The difference between the interferograms, to which we refer as to signal, contains the information about a local piston error. The constant optical path difference (OPD) between the arms equal to the 1/4 of the wavelength is required to distinguish the sigh of the piston. The sufficiently large pinhole diameter, ~1 arcsec for the wavelength 0.5μm, helps to filter out all low order wavefront aberration, including the atmospheric, and leave only the very high frequencies produced by a piston step. The more detailed description of the principal and study of the different errors may be found elsewhere [8].

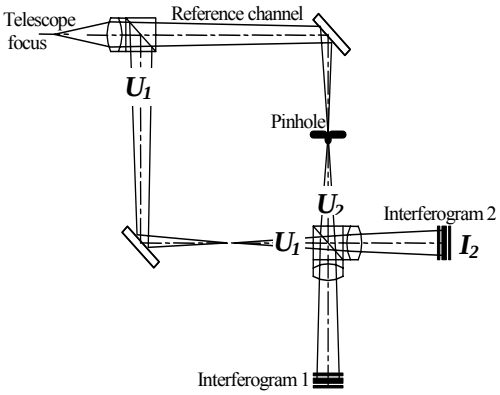

Figure 1. Schematic representation of the Mach-Zehnder interferometer

Figure 2 shows the experimental setup. A source simulator consists of a fiber-fed super-luminescent diode (S), turbulence simulator (A) and segment simulator (B). The setup includes the interferometer (MZ) and two detectors (D1, D2). The turbulence simulator is a duplicate of the reflective rotating phase mask developed at GEPI (Observatoire de Paris) for performance tests of the VLT-NAOS instrument [11]. The scaling of the screen is such that a typical rotational rate of 20 RPM simulates a wind speed of 64m/s. The segment simulator, also developed by GEPI, consists of 25-mm diameter mirrors onto which a hexagonal patch of a certain thickness is deposed. This patch represents a dephased segment. Six such mirrors are mounted in a wheel, with a different patch thickness: -30nm, 0nm, 30nm, 75nm, 150nm, and 230nm. Flat-to-flat segment dimension is 10mm. The interferometric analysis of one of the plates is shown in Figure 3. The low-order phase variations observed are mainly due to the measurement setup.

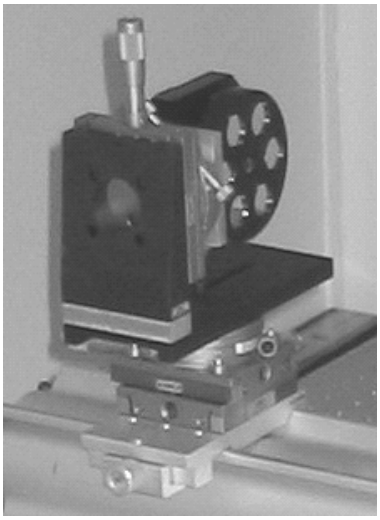

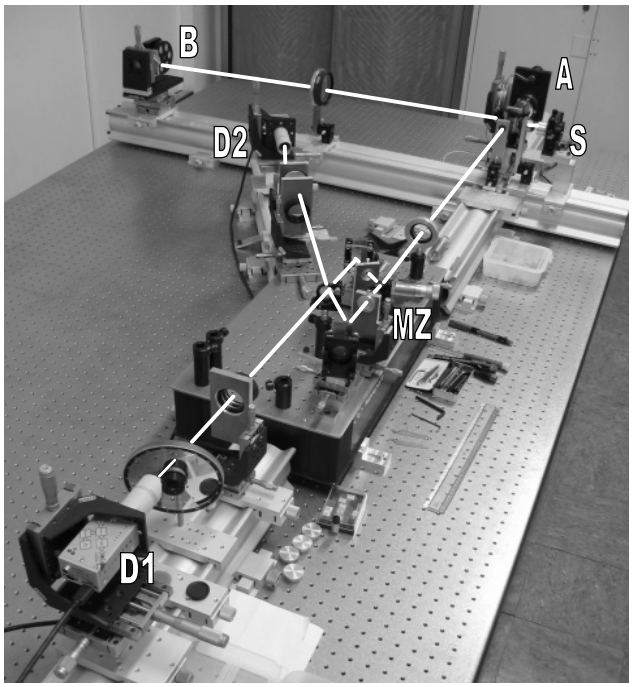

Figure 2. Photograph of the experimental setup (right) and detail of a segment simulator assembly (left).

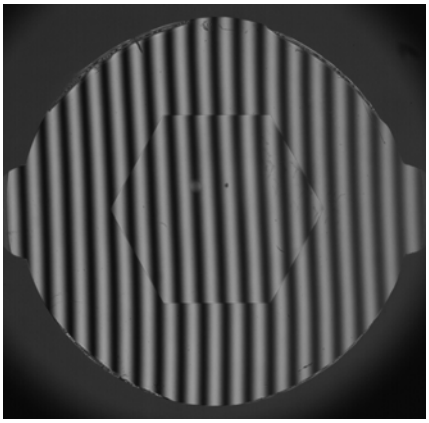

Figure 3. Result of the interferometric analysis of the 75nm segment plate

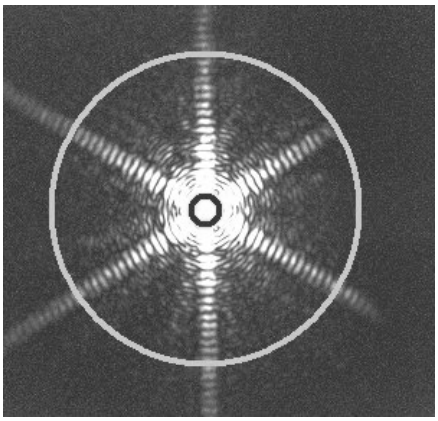

Figure 4. Point spread function formed by a segment plate.

Figure 4 shows a highly saturated star image formed by a mirror with a phase patch. The six diffraction lines due to the hexagonal patch are clearly seen. However, the two lines stretching out to the right are vignetted, and although this vignetting has been reduced to some extent, some will always occur. To avoid the image skewness caused by this vignetting a much larger pinhole is introduced in the second arm (indicated in a big circle in the Figure 4). While this has an additional effect of avoiding the sharp features of the Mach-Zehnder signal, it also reduces the peak signal values, and the effect must be included in simulations in order to produce the comparable results.

A camera is located at each output of the interferometer, but technical restrictions have not allowed us to take simultaneous images at the two outputs as it was planned. We have therefore been forced to investigate the use of a single-output (I), using supplementary images (I_1 and I_2) obtained by blocking in turn each of the two arms to normalize the interferograms:

$$S = \frac{I - (I_1 + I_2)}{\sqrt{I_1 I_2}} \tag{1}$$

This signal, obtained in this procedure, is identical to the one obtained as a difference between two outputs. Although it is less efficient in terms of throughput, it may turn out to be easier to implement practically than the dual-output version. Three images (I, I_1 and I_2) and the processed image (S) are shown in Figure 5.

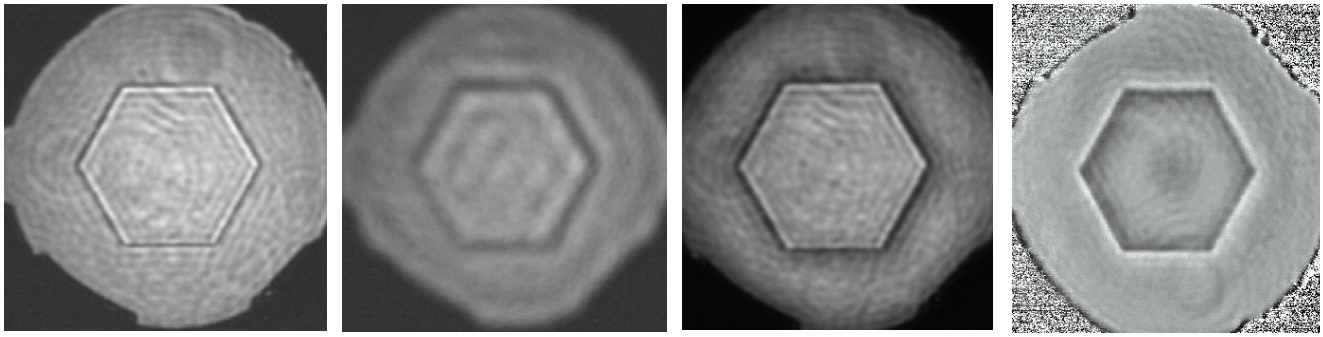

(a) (b) (c) (d)

Figure 5. Measured intensity distribution of arm 1 (a), arm 2 (b), the interferogram (c), and of the normalized signal (d).

2.2 Experimental results

Apart from the difficulties involved with aligning the Mach-Zehnder interferometer in terms of tilts, shear, and location of the zero optical path difference (OPD), the most delicate operation is the fine OPD adjustment to $\lambda/4$ to within some $\lambda/20$, corresponding to a mirror displacement precision of ~10nm at 630nm. To achieve such extremely fine adjustments, one of the mirrors within the interferometer is mounted on a translation stage, equipped with a differential micrometer screw, whose axis is nearly parallel with the mirror surface. This provides a 150-times reduction in the axial mirror movement, giving a displacement of 6.5nm per 1µm micrometer graduation. Thermal stability and air movements also become important in this context, and although ad-hoc measures were taken to limit air fluctuations within the interferometer, this demonstration experiment does not provide the nanometric stability that would be required of an operational instrument.

In Figure 6 (a, b) we plot the normalized profiles (intensity of the signal *S* across the border) obtained by simulation for the different OPD values (a), compared with the experimentally obtained profiles (b). Note that for the OPD equal to $\pi/2$ the amplitude of the signal and the antisymmetry of the signal with respect to the segment boundary achieve the maximum. Plotting the peak-to-valley (PTV) of the signal amplitude against the OPD (Figure 6 c, solid line) shows that its variation is slow close to $\pi/2$; the error is less than 10% for OPD within $\pm\pi/8$. Also, deviations from the optimal OPD are nearly proportional to the mean signal level (Fig. 6 c, dash line), allowing potentially correcting the signal amplitude within a wide range of OPDs. Four our lab tests, a procedure for OPD adjustment based on real-time display of the average image intensity has been devised and proven to give good results.

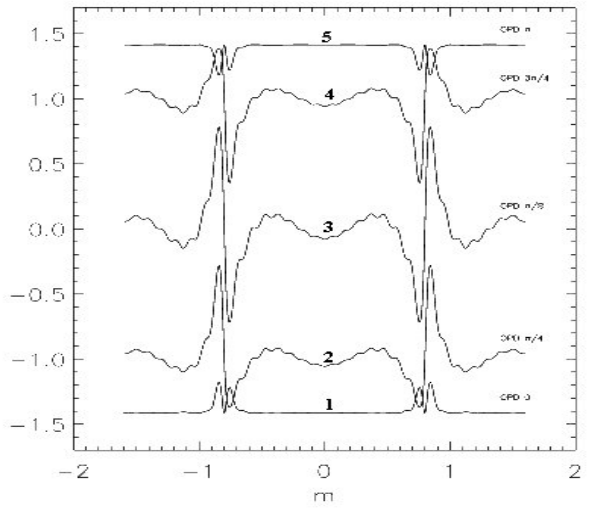

(a)

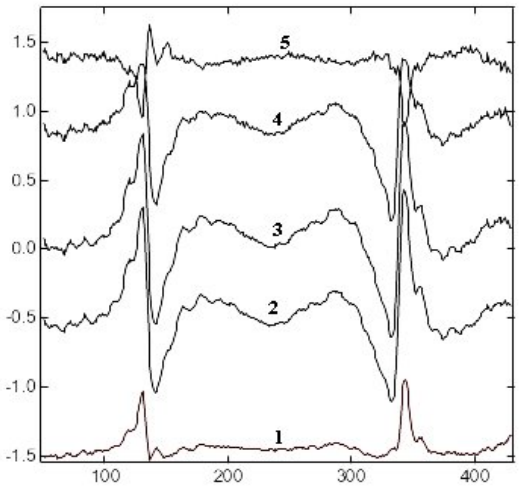

(b)

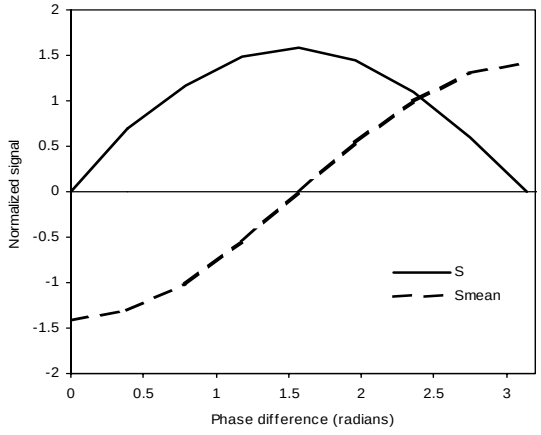

(c)

Figure 6.

Upper: Simulated (a) and experimental (b) signal profiles for different OPD adjustments using a piston step of 75nm. Curve 1: OPD=0; curve 2: OPD=$\pi/4$; curve 3: OPD= $\pi/2$; curve 4: OPD= $3\pi/4$; curve 5: OPD= π.

Left: Plot of the PTV signal (solid line) and the mean signal level (dash line) against OPD

2.3 Performance without atmosphere

Figure 7 (a and b) compares the simulated and the measured signal profiles in the absence of atmospheric turbulence for each of the five piston plates. Experimentally, this configuration is obtained by replacing the turbulence simulator with a flat mirror. While the correspondence is good for small piston values, the signal for the two larger steps is somewhat different. Figure 7 (c) gives a more quantitative analysis of these results, representing the average PTV values for each piston step (symbols) compared with theoretical expectation (full line). Two series of 10 images are taken, one with OPD = +λ/4, and one with OPD = -λ/4, and a vertical profile containing two steps (edge 1 and 2) is extracted from each image from which PTV values are measured and then averaged; vertical error bars indicate standard deviations. A good correspondence for the three smallest piston values is seen, but the behavior for larger steps is somewhat curious. While the change in OPD is of little influence on the results, indicating that the reproducibility of the OPD adjustment procedure is sufficient, the difference between the two segment edges is large. This effect is not yet understood, but the contributing factors are thought to include shearing, pupil focus, and residual vignetting effects.

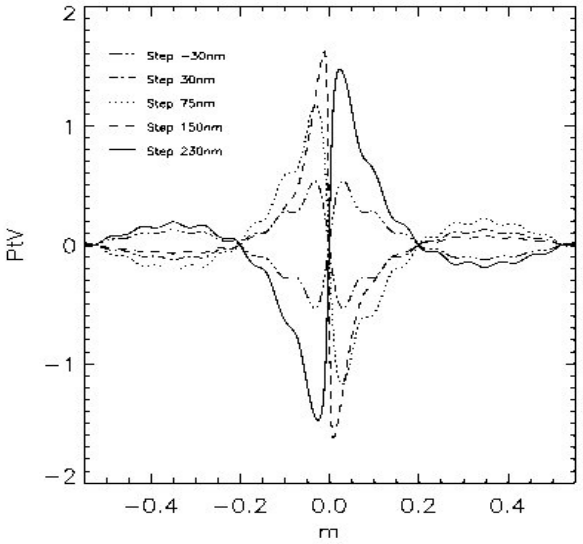

(a)

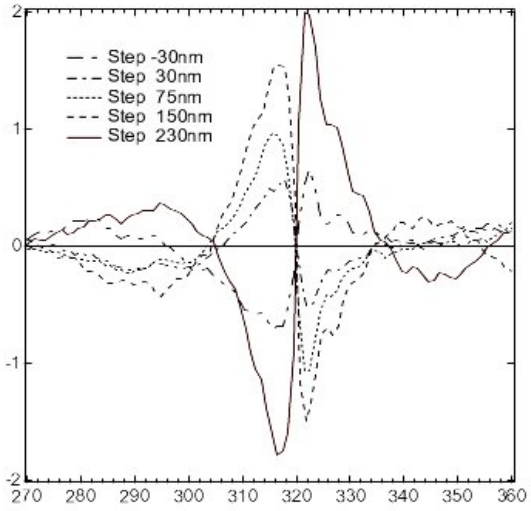

(b)

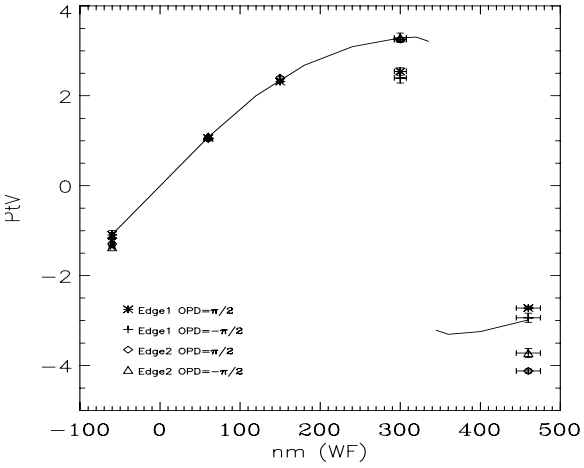

(c)

Figure 7.

Upper: Simulated (a) and experimental (b) signal profiles for one border of each segment without atmosphere.

Left: Comparison of the averaged experimantal PTV signal amplitude (symbols) with simulated data (line) .

2.4 Performance with atmosphere

Installing the rotating turbulence simulator allows realistic performance testing of the method. However, it was soon noticed that the simulated turbulence varied strongly as a function of angular position. The variation was quantified by calculating the Fried parameter (r_0), estimated from the FWHM of Gaussian fits to the measured PSFs, from 22 short-exposure images. Figure 8 shows a histogram of the r_0 values obtained, indicating that instead of a typical value of 20cm, the mean seeing is equal to 64cm, with peaks reaching 2m. The mean seeing level is not a serious problem, since it is just a matter of scaling between segment size and a turbulence screen. However, as we will see, the strong variability of the instant seeing appears to contribute to the difficulty of comparing observations and simulations. For the long exposure images (1 second), representing approximately one third of a screen rotation, the mean seeing was estimated to 61 cm with a standard deviation of 11cm (Figure 8, dashed line). A qualitative comparison between simulation and measurements (Figure 10) indicates very good correspondence between the two, but a quantitative analysis (Figure 9) gives a more complex picture. Compared with the measurements without seeing, results for the small piston values have much larger variability and are generally below the expected values. A better fit is obtained for the two larger piston steps, but only at the cost of even larger variability.

In addition to the problems mentioned above for the case without turbulence, it seems that the problems encountered here may be due to the large variability of the instantaneous seeing condition. While the simulations are made using a sequence of 1000 independent phase screens each created using identical turbulence statistics, 1-second exposures with our turbulence simulator corresponds to some 120 independent phase screens with largely different statistics. As one can see from the simulated curves in Figure 10, the turbulence statistics has a great influence on the signal PTV, especially for large piston steps.

Another error source is related to the atmospheric tip-tilt error, causing time-variable misalignment between the pinhole and the seeing disk. Problematic in itself, this effect is aggravated by the fact that the three images used to construct the Mach-Zehnder signal are not taken simultaneously. Although the effect should be reduced by increasing the exposure time, it may be interesting to consider the use of a real-time tip tilt corrector in a practical implementation of this concept.

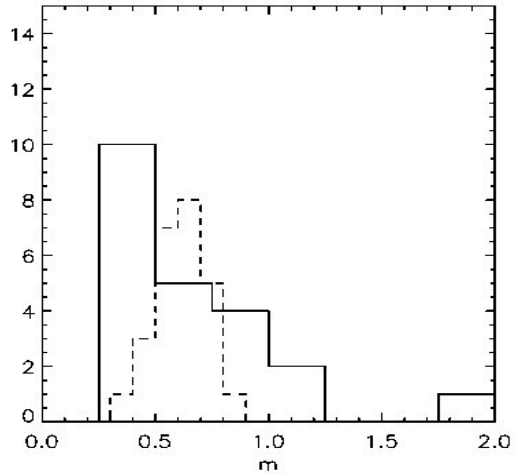

Figure 8. Seeing statistics for our atmospheric turbulence generator in the case of short exposures (solid line) and long exposures (dash line).

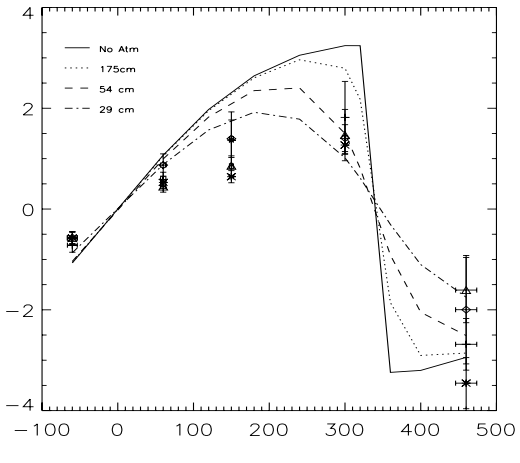

Figure 9. Comparison of the averaged experimental PTV signal amplitude (symbols) with simulated data (lines) for different atmospheric conditions.

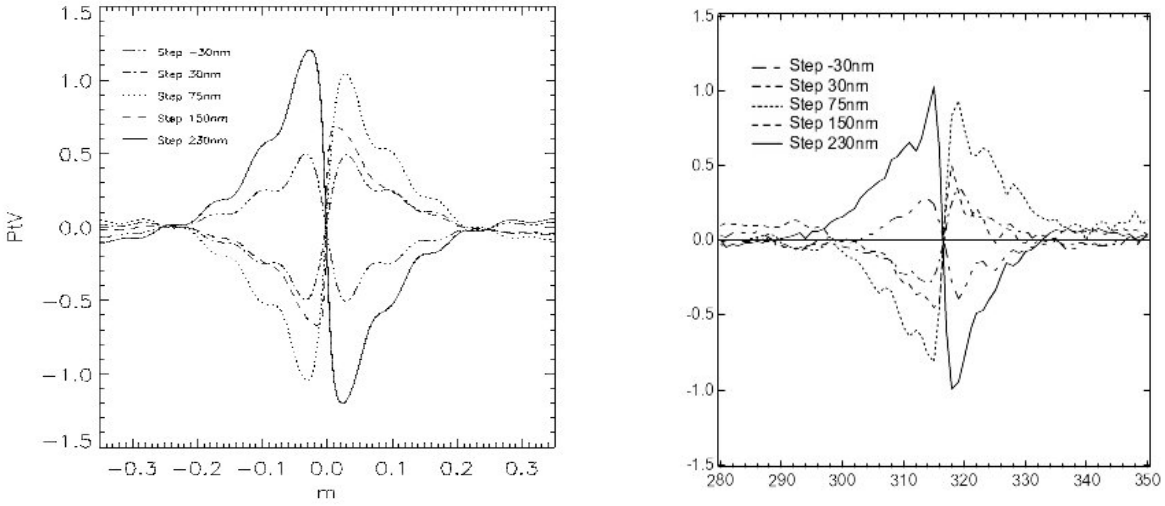

(a) (b)

Figure 10. Simulated (a) and experimental (b) signal profiles for one border of each segment with atmosphere.

3. CLOSE LOOP SIMULATION

So far we considered the particular properties of the Mach – Zehnder interferometer. However, the signal retrieval algorithm for phasing close loop for the multi-segmented mirrors is general for all phasing techniques. It is based on the symmetric and anti –symmetric properties of the signal. In the following we describe this method together with the close loop results for the case of the Mach – Zehnder interferometer. In the cases of a curvature sensor and a pyramid sensor the functions J_1 and J_2, introduced below, will have different analytical expression keeping the same general properties.

3.1 Signal symmetric and anti-symmetric properties

One of the most important features uniting all phasing techniques is the localization of the signal near the intersegment boundary. That means that one can retrieve the relative phase step between two adjacent segment by measuring the signal only near the given boundary. Of course to phase the whole segmented mirror one has to measure the relative phase step over all boundaries and then use the matrix algebra to calculate piston, tip and tilt for each segment. The close loop algorithm based on Singular Value Decomposition (*SVD*) is described later.

Let consider a given boundary and bound with it local Cartesian coordinate system: axis *y* coincides with the boundary and axis *x* goes through the segments' centres. Six independent values describe an arbitrary segment configuration in this coordinates. Phase piston on the left segment (in the half plane $x<0$) is φ_1. This segment rotates by a physical angle δ_{1x} about the axis which is parallel to the *y* axis and goes through the center of the segment. A rotation angle about the *x* axis is δ_{1y} The segment in the half plane $x>0$ has a phase piston φ_2 and rotates by an angle δ_{2x} about the axis parallel to the *y* axis and by an angle δ_{2y} about the *x* axis. Although at this point we speak about the relative displacements of two segments and could set φ_1 equal zero, nevertheless it is more convenient to keep a zero phase offset with respect to the whole mirror as a shift of the central segment for example. For the following calculation it is convenient to express all values through the wavefront aberration component. The phase errors in the segment center due to the corresponding segment bent are: $s_{1x} = 2\pi\delta_{1x}d/\lambda, s_{2x} = 2\pi\delta_{2x}d/\lambda, s_{1y} = 2\pi\delta_{1y}d/\lambda, s_{2y} = 2\pi\delta_{2y}d/\lambda.$

The expression for the Mach-Zehnder signal as function of piston, tip and tilt aberrations is [12]:

$$S(x,y) = \begin{cases} \sin[\Delta\varphi(x,y)]\,\mathrm{Re}\,J_2(x) + \mathrm{Im}\,J_1(x) - \cos[\Delta\varphi(x,y)]\,\mathrm{Im}\,J_2(x), & x < 0 \\ \sin[\Delta\varphi(x,y)]\,\mathrm{Re}\,J_1(x) + \mathrm{Im}\,J_2(x) - \cos[\Delta\varphi(x,y)]\,\mathrm{Im}\,J_1(x), & x >= 0 \end{cases} \quad (2)$$

where

$$\Delta\varphi(x,y)=\frac{2x}{d}(s_{2x}-s_{1x})+\frac{2y}{d}(s_{2y}-s_{1y})+(\varphi_2-\varphi_1)-(s_{1x}+s_{2x}), \tag{3}$$

d is a segment flat to flat width, λ is a wavelength. If the pinhole has a apodization of transmission with the Gaussian profile, the function J_{12} is expressed through a error function of a complex argument as:

$$J_{12}=\mathrm{sign}(x)\exp\left[-\frac{s_{12x}^2+s_{12y}^2}{(db)^2}\right]\left[1-\Phi\left(b|x|+i\frac{s_{12x}}{db}\right)\right]. \tag{4}$$

Parameter *b* is related to the pinhole full width half maximum *a* of the Gaussian pinhole as $b=0.6\pi a/\lambda$. Real and imagery parts of J_{12} are shown in Figure 11. For the case of the round pinhole, as well as for two other types of the segment error sensors J_{12} are not anymore expressed through the error function, but have the similar general behavior.

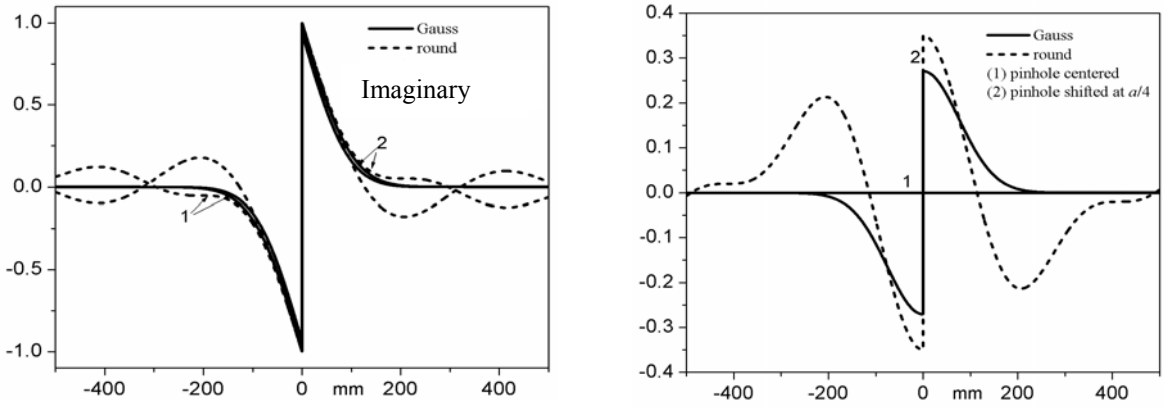

Figure 11. Real and imaginary parts of the function J_{12}. Curve 1: no tilts, curve 2: $s_x=0.4db, s_y=0$. For the zero tilts the imaginary part is zero.

In a case of the small errors the linear approximation for the signal is

$$S(x,y)\approx\Delta\varphi(x,y)\mathrm{sign}(x)\left[1-\Phi(b|x|)\right]. \tag{5}$$

From Eqs. 3 and 5 it follows that the information about the difference $\varphi_2-\varphi_1$ and the sum $s_{2x}+s_{1x}$ is contained in the antisymmetric component of the signal with respect to the *y* axis, the difference $s_{2x}-s_{1x}$ is in the symmetric component with respect to the same axis, and the difference $s_{2y}-s_{1y}$ is in the antisymmetric component with respect to the *x* axis. The area of signal localization we split into four identical zones as shown in Figure 12 a and integrate the signal S(x, y) within each of this zone, calculating the integral values

$$I_n=\int_{\varepsilon_n}S(x,y)dxdy, \quad n=1...4. \tag{6}$$

Using these values we define three integral criteria: K_0 – symmetry coefficient with respect to *y* axis; K_1 – antisymmetry with respect to *y* axis and K_2 – antisymmetry with respect to *x* axis:

$$K_0=(I_1+I_2+I_3+I_4);\quad K_1=(I_1+I_4)-(I_2+I_3);\quad K_2=(I_1+I_3)-(I_2+I_4) \tag{7}$$

It can be seen that from Eq. 5 that each criterion is responsible for different aberrations:

$$K_0\sim s_{2x}-s_{1x},\quad K_1\sim(\varphi_2-\varphi_1)-(s_{2x}+s_{1x}),\quad K_2\sim s_{2y}-s_{1y}. \tag{8}$$

With the increase of the segmentation errors the criteria K_n are not anymore the linear functions and their dependence on the different aberrations cannot be easily disentangled. Criteria K_n for the large rang of aberration values are shown in Figure 12 b. Criterion K_1 is a periodical sine function of the phase step, and the range of the measurable phase difference therefore is limited to [-π/2, π/2]. This problem, also called "π – ambiguity" appears in all co-phasing methods operating in a monochromatic regime. Within this capture range the phase can be reconstructed unambiguously. If the initial piston difference is beyond this limit, the segments may be phased not to the zero step, but to the integer number of wavelengths.

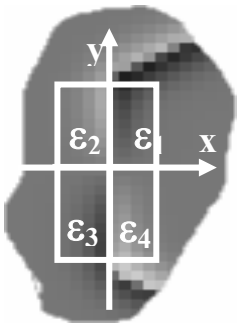

Figure 12a. Signal analysis.

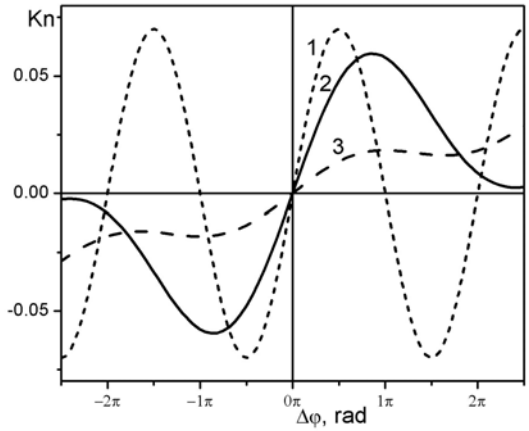

Figure 12b. Behaviour of the criteria K_n. Curve 1: Criterion K_1 for the pistons only. Ordinate K_1; abscissa $\varphi_1-\varphi_2$. Curve 2: Criterion K_2 for the difference of the y-tilts only. Ordinate K_2; abscissa $s_{2y} - s_{1y}$. Curve 3: Criterion K_0 for the sum of x-tilts only. Ordinate K_0; abscissa $s_{2x} + s_{1x}$.

3.2 Segmented mirror eigenmodes

In a sense of the reconstruction of the segmented mirror surface the criteria K_0, K_1, and K_2 are analogous to the measurements provided by the edge sensors. In the existing [4] phasing systems two capacitive sensors, placed on each border of the segment, provide the information about the relative intersegment shifts. The sum of these two sensors readings is relevant to the piston between two segments and difference of two x-tilts. The difference between the readings contains the information about a relative y-tilt. That is completely analogous to the K_1 and K_2 criteria. Some edge sensors measure also the solid angle between segments or the sum of x –tilts, although with less sensitivity. This parameter is analogous to the criteria K_0, which is also much less sensitive to $s_{2x} + s_{1x}$ than K_1 to $\varphi_1-\tilde{\varphi}_2$ or K_2 to $s_{2y} - s_{1y}$ (Fig. 12b).

A vector $\mathbf{u} = \{K_{01}, K_{11}, K_{21}, \ldots K_{0i}, K_{1i}, K_{2i}, \ldots K_{0m}, K_{1m}, K_{2m}\}$, where m is the number of boundaries, forms a signal vector. An actuator vector consists of n triplets: three actuators v_{0i}, v_{1i}, v_{2i} for each segment, where n is a total number of segments: $\mathbf{v} = \{v_{01}, v_{11}, v_{21}, \ldots v_{0i}, v_{1i}, v_{2i}, \ldots v_{0n}, v_{1n}, v_{2n}\}$. The actuator vector **v** is related to the sensor vector **u** by the linear mapping represented as a two dimensional matrix **A**:

$$\mathbf{A}\mathbf{v} = \mathbf{u}\,. \tag{9}$$

An optimum modal correction requires the expansion of the signal u in an orthonormal set generated by SVD:

$$\mathbf{A} = \mathbf{U}\mathbf{\Sigma}\mathbf{V}^{\mathrm{T}}\,. \tag{10}$$

The 3n column vectors of **U** and **V** form orthonormal sets $\{\mathbf{u}_j\}$ and $\{\mathbf{v}_j\}$ correspondingly. Symbol $^{\mathrm{T}}$ denotes transpose. The matrix **V** defines an orthonormal basis for the system, i.e. segmented mirror modes. Any configuration of the segments can be expressed as a linear combination of those modes. The matrix **Σ** is diagonal and contains 3n singular values σ_j. Its value defines the sensitivity of the system to the mode with index j. So the modes which present the global mirror piston, global tip and tilt will have the singular value σ_j equal zero, because in these three aberrations there is no any relative segment shifts. Also the mode which corresponds to the global defocus will have a singular value very low, because it is formed only by the solid angle between segments and hence only criterion K_0 contributes in the measurement.

In the modal control matrix **A** is found in calibration. The control matrix **B**, which finds the actuator vector by a signal vector and is inverse to **A**, is obtained as

$$\mathrm{B} = \mathbf{V}\mathbf{\Sigma}^{-1}\mathbf{U}^{\mathrm{T}}\,. \tag{11}$$

The diagonal matrix $\mathbf{\Sigma}^{-1}$ consists of the values σ_j^{-1}. To exclude the least sensed modes with zero or very small singular values, the corresponding σ_j^{-1} in *SVD* are replaced by zero. The threshold depends on the value of noise in the system, because σ_j^{-1} defines also the noise propagation from signals to actuators.

The difference between control provided by the edge sensors and the optical method is the signal vector **u**. The mirror modes $\{\mathbf{u}_j\}$ are the same as for the edge sensor as well as for the optical sensor if the configuration of the mirror is the same. So the performance of each of the methods can be analysed by a studying the singular values σ_j., which define the sensitivity to the modes and the noise propagation.

We simulated a segmented mirror consisted of 91 segments organized in 5 hexagonal "rings". Pushing each segment by a given value for piston, tip and tilt and calculating the criteria K_n, we constructed the calibration matrix. The area for signal analysis (Fig. 12 a) was chosen to be square with the side $d/6$, where d is a segment flat to flat width. Applying a standard *SVD* algorithm on the calibration matrix, we obtained the eigenmodes and the singular values. The nine of the modes are shown in Figure 13, the singular values – in Figure 14. The low order modes are close to the classical optical aberrations – piston, tip-tilt, defocus, astigmatism, coma and etc. Piston, tip and tilt are not sensed by the system. The corresponding singular values are zeros. The defocus mode has a very low singular value $3 \cdot 10^{-3}$ with respect to the highest singular value.

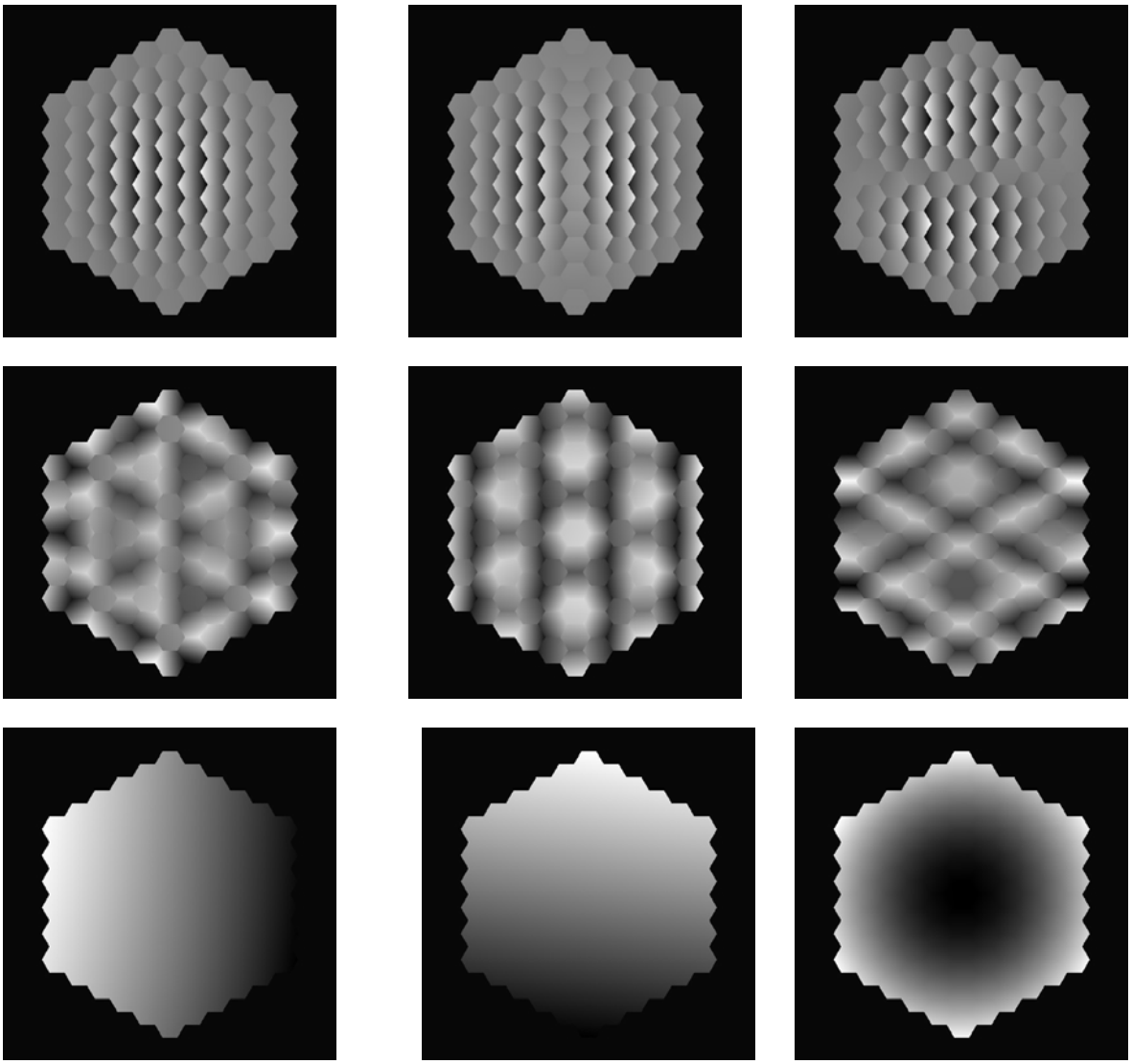

Figure 13. Nine out of 273 eigenmodes of the segmented mirror. The upper line is three highest modes with indexes 273, 272 and 271; in the middle – modes with the indexes 43, 42 and 41; and on the bottom: tip-tilt and defocus with the indexes 2, 3 and 4.

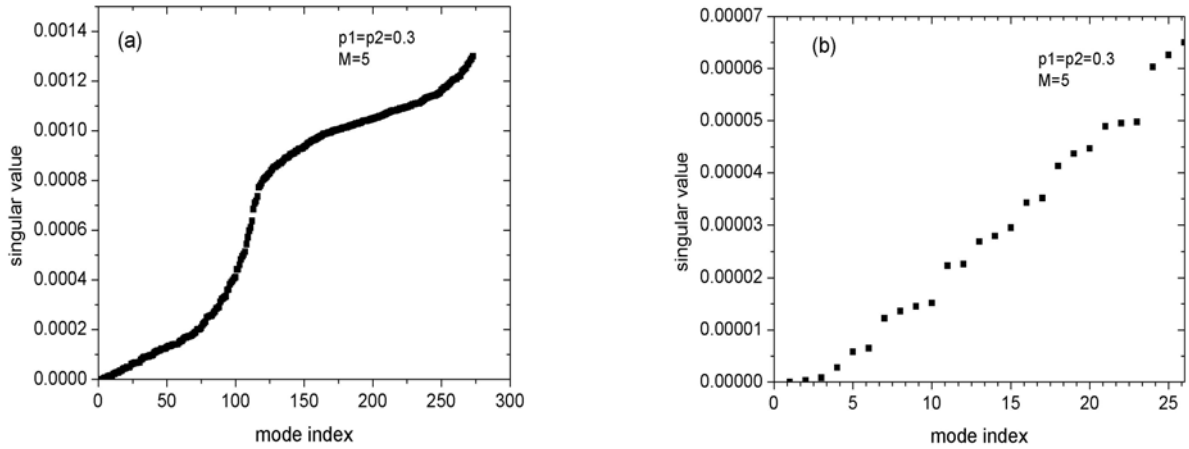

(a) (b)

Figure 14. Singular values for the segmented mirror with 91 segments for all 273 eigenmodes (a) and for the last 26 modes with the lowest eigenvalues. Calculations include piston and tip-tilt for each segment.

Some telescopes use a separate method to correct for the tip-tilt of the segment, for example Schack – Hartmann sensor. Then the phasing camera is responsible only for the segment piston measurement. In this case only criterion K_1 is required. Among the mirror modes formed only by segment pistons one may recognize pseudo-defocus and pseudo-tip-tilt (Figure 15). Unlike the normal defocus and tip-tilt these ones are sensed by the system, because they are formed not by the solid angles between segment, but by the intersegment steps. The ratio between a singular value corresponding to the pseudo defocus to the highest singular value is 0.2. For the pseudo tip and tilt it equals 0.15.

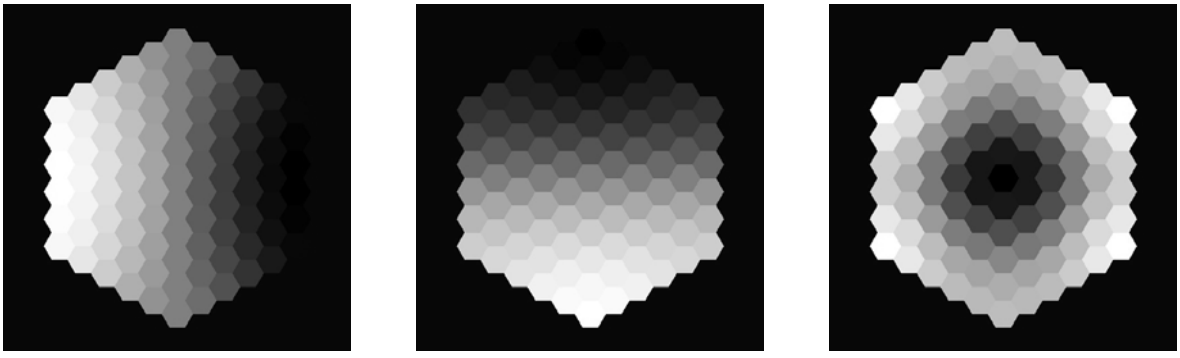

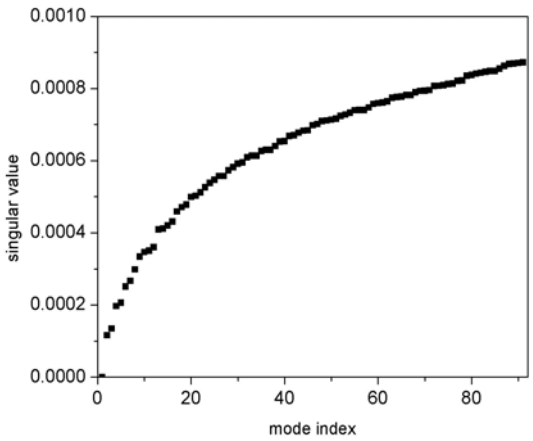

Figure 15.

Upper: Tip-Tilt and defocus formed by segment pistons

Left: Singular values for the segmented mirror with 91 segments. Calculations include only piston for each segment.

3.3 Close loop results

To close the loop we used the control matrix **B** given by Eq. 11. We did not introduce any additional noise into the system. The simulation was performed in the monochromatic regime with the wavelength equal to 500nm. The result of phasing strictly depends on the initial rms. In Figure 16 we present a mirror rms evolving with the iterations for the piston phasing only, as well as initial phase and the final phase for the large initial rms. For the small initial rms the residual wavefront is flat. If the initial rms is low all segment piston are within the capture range and in the result the zero error is achieved. With an increase of rms some segments are outside the capture range. They are "phased" to the nearest wavelength. As the result the initially randomly de-phased mirror contains some segments shifted by the integer number of the wavelength. To overcome this problem the multi -wavelength technique may be used.

In a case of piston and tip-tilt errors the situation is similar (Figure 17). Although in this case the capture range exists also for the tip – tilt value. We did not simulate the work of the active optics which would correct for the global tip, tilt and defocus. Consequently, for the initially small rms the mirror is phased to the mode which is a linear combination of tip, tilt and defocus. For the large initial rms some other low order modes remain and the process diverges.

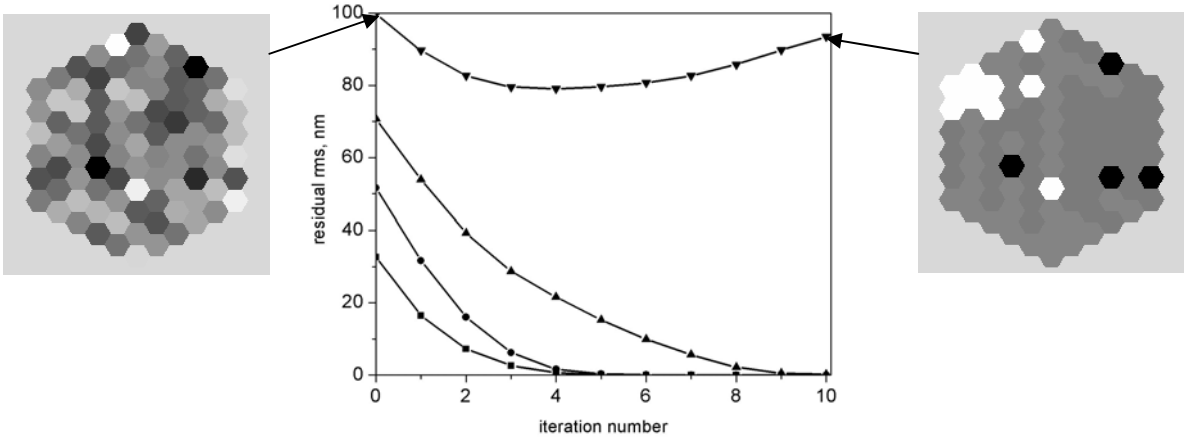

Figure 16. Close loop on phasing for the piston error only for the different initial rms values. Initial and final segment errors distributions are shown for the case of a large initial rms.

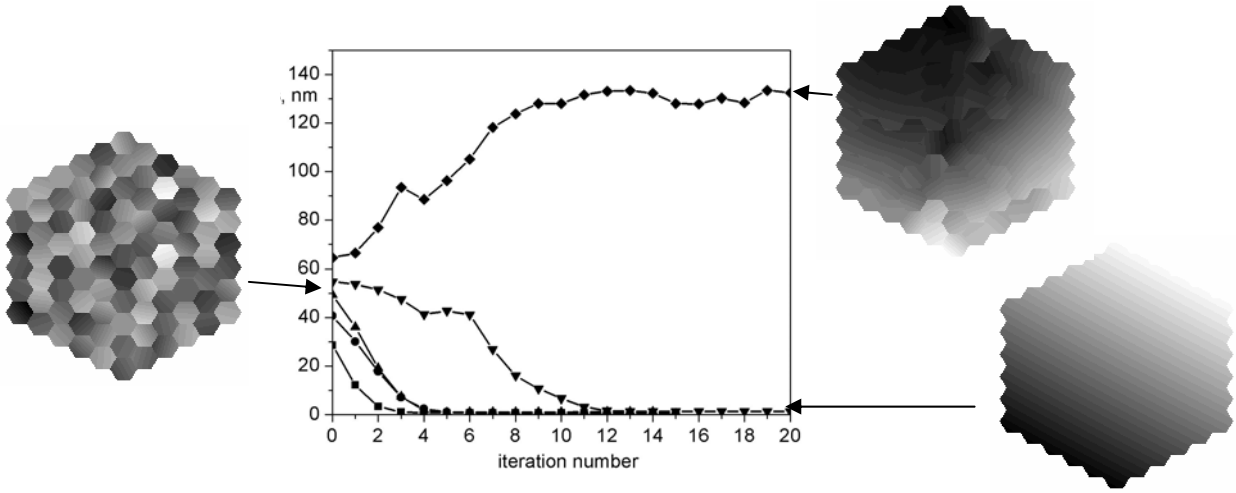

Figure 17. Close loop on phasing for the piston, tip and tilt error for the different initial rms values. Initial and final segment errors distributions are shown for the case of a small and large initial rms.

4. CONCLUSION

Several optical methods for phasing of segmented mirrors are being demonstrated experimentally and by simulations. We presented the one based on the Mach – Zehnder interferometry. The signal predicted by theory and in computer simulations was observed experimentally in both with and without atmospheric turbulence. The behavior of the signal on the intersegment step and the parameters of the system is in a good agreement with the theory and simulations.

The calculation of the symmetric and antisymmetric components of the signal makes an algorithm for the segment error retrieval analogous to the measurement with the use of the edge sensors. Both methods provide the same set of mirror eigenmodes and show the same general behavior of singular values. This fact makes the mirror control technique in both cases equivalent. The system is more sensitive to high order segmentation modes. They are corrected first. The low order modes are less easily sensed. These modes, which correspond to the classical optical aberrations, may remain uncorrected.

The main concern, which is general for all optical approaches to segment phasing, is the limited capture range. Even with an initial wavefront rms of $\lambda/5$ some segments happen to be outside the capture range of $\pm \lambda/4$. In the closed loop control algorithm used, these segments are driven towards a one-lambda difference with respect to their neighbors. In this respect, a more thorough study of the properties and eigenmodes of segmented mirrors, together with developing more accurate close loop control algorithms, is required.

ACKNOWLEDGMENTS

The authors wish to acknowledge that this research is supported by the European Commission RTN program: "Adaptive Optics for the Extremely Large Telescopes", under contract #HPRN-CT-2000-00147.

REFERENCES

1. E.T Brunetto, P. Dierickx, R. Gilmozzi, G.J. Monnet, “OWL phase A status report”, 5489-23 at this conference.
2. G. Chanan and M. Troy, “Strehl ratio and modulation transfer function for segmented mirror telescope as function of segment phase error,” Appl. Opt. 38, pp. 6642-6647 (1999).
3. N. Yaitskova, K. Dohlen, P. Dierickx, “Analytical study of diffraction effects in extremely large segmented telescopes” JOSA A/Vol. 20, No. 8, pp. 1563-1575 (2003).
4. J.N. Aubrun, K.R. Lorell, T.W. Havas, and W.C. Henninger (1988). "Performance analysis of the segmented alignment control system for the ten-meter telescope," Automatica, vol. 24, pp. 437-454.
5. S. Cuevas, V.G. Orlov, F. Garfias, V. Voitsekhovich and L. Sanchez, “Curvature equation for a segmented telescope,” in *Optical Design, Materials, Fabrication, and Maintenanc*e, P. Dierickx, ed., Proc. SPIE **4003**, 291-302 (2000).
6. A. Schumacher and N. Devaney, “DIPSS: cophasing segmented mirrors with minimal hardware requirement”, in preparation.
7. S. Esposito, E. Pinna, A. Tozzi, P. Stefenini, N. Devaney, “Co-phasing of segmented mirrors using pyramid sensor”, in *Astronomical Adaptive Optics Systems and Applications*, R. K. Tyson, M. Lloyd - Hard, eds., Proc. SPIE **5169**, pp. 214-225 (2003).
8. N. Yaitskova, “Performance analysis of Mach – Zehnder interferometer for detection of wavefront discontinuities”, in *Astronomical Adaptive Optics Systems and Applications*, R. K. Tyson, M. Lloyd - Hard, eds., Proc. SPIE **5169**, pp. 62-71 (2003).
9. L. Montoya, N. Yaitskova, P. Dierickx, K. Dohlen “Mach-Zehnder wave front sensor for phasing of segmented telescopes”, in *Future Giant Telescopes*, J. R. P. Angel and R. Gilmozzi, eds., Proc. SPIE **4840**, pp. 564-573 (2002).
10. F. Gonte, N. Yaitskova, P. Dierickx, A. Courteville, S. Esposito, N. Devaney, K. Dohlen, M. Ferrari, L. Montoya, “APE: a breadboard to evaluate new phasing technologies for a future European giant optical telescope,” 5489-144 at this conference.
11. K. Dohlen, A. Origné, D. Pouliquen, B. Swinyard, "Optical design of the SPIRE instrument for FIRST", in UV, optical, and IR space telescopes and instruments, J. B. Breckinridge, P. Jacobsen, Eds, Proc. SPIE **4013**, pp. 119-128 (2000).
12. N. Yaitskova, K. Dohlen, P. Dierickx, “Mach-Zehnder Interferometer for Phasing Segmented Telescopes: Theory and Analytical Treatment”, in preparation.